iScience

Article

Wireless charging LED mediated type I photodynamic therapy of breast cancer using NIR AIE photosensitizer

Highlights

- Wireless charging was used to solve the light penetration issue
- The proposed AIE photosensitizer exhibited efficient type I ROS production
- This photosensitizer-device combination treated tumors with good biosafety

Authors

Chengbin Yang, Shiqi Tang, Qiqi Liu, ..., Gaixia Xu, Xiaoyan Chen, Zhourui Xu

Correspondence

chenxiaoyan@cuhk.edu.hk (X.C.), xuzhouray@szu.edu.cn (Z.X.)

In brief

Materials in biotechnology; Optical property; Biomaterials

Yang et al., 2025, iScience *28*, 112196
April 18, 2025
https://doi.org/10.1016/j.isci.2025.112196

CellPress

iScience

CellPress
OPEN ACCESS

Article

Wireless charging LED mediated type I photodynamic therapy of breast cancer using NIR AIE photosensitizer

Chengbin Yang,[1] Shiqi Tang,[1] Qiqi Liu,[1] Miaozhuang Fan,[1] Wenguang Zhang,[1] Yingyu Liu,[2] Xin Chen,[1] Gaixia Xu,[1] Xiaoyan Chen,[2,*] and Zhourui Xu[1,3,*]

[1]School of Biomedical Engineering, Shenzhen University Medical School, Shenzhen University, Shenzhen 518055, China
[2]Maternal-Fetal Medicine Institute, Department of Obstetics and Gynaecology, Shenzhen Baoan Women's and Children's Hospital, Shenzhen 518133, China
[3]Lead contact
*Correspondence: chenxiaoyan@cuhk.edu.hk (X.C.), xuzhouray@szu.edu.cn (Z.X.)
https://doi.org/10.1016/j.isci.2025.112196

SUMMARY

Due to limited light penetration and dependence on oxygen, photodynamic therapy (PDT) is typically restricted to treating shallow tissues. Developing strategies to overcome these limitations and effectively using PDT for tumor treatment is a significant yet unresolved challenge. In this study, we present a smart approach combining a wireless-charged LED (wLED) with a type I aggregation-induced emission photosensitizer, MeOTTMN, to address both light penetration and tumor hypoxia issues simultaneously. MeOTTMN, characterized by twisted molecular architecture and strong intramolecular electron donor-acceptor interaction, produces high levels of hydroxyl and superoxide radicals and emits near-infrared light in its aggregated state, thus facilitating fluorescence imaging-guided PDT once formulated into nanoparticles. The inhibition of breast cancer xenografts provides compelling evidence of the treatment efficacy of type I PDT irradiated through an implantable wLED. This strategy provides a conceptual and practical paradigm to overcome key clinical limitations of PDT, expanding possibilities for clinical translation.

INTRODUCTION

Photodynamic therapy (PDT) represents a minimally invasive yet highly effective therapeutic approach compared to conventional modalities.[1,2] Upon exposure to light irradiation, the excited photosensitizers (PSs) will interact with oxygen-containing substrates and generate highly oxidizing reactive oxygen species (ROS), thereby enabling the treatment of pathological cells.[3–6] Currently, PDT is clinically approved for treating several early cancers and residual tumors in the superficial biological tissues, such as the skin, oral cavity, esophageal, lung, and bladder, showcasing notable therapeutic efficacy.[7–10] Meanwhile, from a fundamental research perspective, PDT has also demonstrated significant potential for treating a broader range of cancer as well as infectious diseases,[11] owing to recent advances in materials science.[12] Nonetheless, such success of PDT has not been promoted to clinical tumor treatment owing to the limited tissue penetration depth of the excitation light[13,14] and the oxygen-scarcity environment of tumors. Exploration of a novel PDT strategy to break the bottleneck and use it in treating deep-seated hypoxic tumors is thus an appealing and significantly meaningful task.

Over the past decade, great efforts have been made to overcome the hurdles in light penetration depth by developing long-wavelength PSs. However, even with excitation light in the second near-infrared (NIR-II) region,[15] the well-documented biological transparent window,[16–18] the maximum penetration depth reported thus far is below 25 mm,[19–21] falling short of the requirements for effective phototherapy in deep tissues. Moreover, considering the energy required for the transition from triplet oxygen to singlet oxygen,[22] PSs excited by NIR light normally have a low yield of ROS, rendering long-wavelength PSs a seemingly unattainable goal.[18] The hypoxia condition in tumors is another critical issue that impacts the therapeutic efficacy of PDT.[23,24] Although quite a few innovative approaches have been reported to increase the intratumoral oxygen level, the untoward side effects, such as hyperoxic seizures,[25] barotrauma problems,[26] and the promotion of cancer cell proliferation,[4] severely compromise the therapeutic potential of PDT. Consequently, unleashing the full potential of PDT in cancer therapy remains a distinct goal and "mission impossible".

As an intervention modality based on the drug-device combination, the potential for deep-tissue PDT may lie in innovations in both light sources and PSs. The advent of wireless-powered technology has breathed new energy into the biomedical field.[27,28] An implantable wireless-powered LED (wLED) could smartly bypass the light attenuation of biological tissues and skin photosensitivity, thereby increasing the light accessibility to deep tumors.[29–31] In addition, such a wLED could be remotely controlled even in freely behaving animals.[32,33] Building on this

foundation, another key issue is how to effectively exert the photodynamic effects within hypoxic conditions. In recent years, type I PSs that can either recycle or without using oxygen to generate superoxide ($O_2^{\cdot -}$) and hydroxyl radicals ($^{\cdot}OH$)[34] have been deemed as a perfect choice to treat hypoxic tumors because they work effectively in hypoxia.[35] Currently, type I PSs with aggregation-induced emission (AIE) characteristics have emerged as ideal options for tumor therapy.[17,36,37] They not only demonstrate superior biocompatibility compared to inorganic PSs but also showcase typical AIE and aggregation-enhanced intersystem crossing (AI-ISC) features, making them particularly effective when used in their aggregated form within physiological environments and facilitating fluorescence imaging-guided PDT.[38] Undoubtedly, exploring advanced photodynamic protocols that combine wLED with type I AIE PSs represents an attractive and promising avenue for deep-tissue PDT.

In this contribution, we revisited the concept of PDT and proposed a new drug-device combination based on type I AIE PS, namely MeOTTMN, and an implantable wLED for continuous PDT of 4T1 breast tumors in freely behaving mice (Scheme 1). Attributed to the twisted architecture and prominent intramolecular electron donor-acceptor (D-A) relationship, the proposed MeOTTMN exhibited strong production rates of $^{\cdot}OH$ and $O_2^{\cdot -}$ under wLED irradiation in the aggregated state. After being formulated into nanoparticles (NPs) and modified with iRGD, MeOTTMN NPs-iRGD (MTDi) exhibited good tumor-targeting ability, evidenced by NIR fluorescence imaging. To perform deep-tissue type I PDT on tumors, wLED was intraperitoneally implanted into tumor-bearing mice and operated under wireless charging. The excellent therapeutic effect of the wireless PDT was evidenced by the growth-inhibited tumors, histological analysis, and various blood tests. Furthermore, the carrying of wLED did not significantly affect the living behaviors and health state of mice. This research represents the first attempt to treat tumors using type I PDT mediated by an implantable wLED, efficiently overcomes the two major hurdles in PDT, and poses good potential to be applied in future clinical translation of deep-tissue PDT.

RESULTS AND DISCUSSION

Photophysical property studies

The compound MeOTTMN is designed with a typical D-A structure incorporating various core components: a methoxy-modified triphenylamine (MeOTPA) moiety serving as a strong electron donor, thiophene working as an additional electron donor and π-bridge, and two cyano units working as electron acceptors.[39] This configuration results in a strong D-A strength with extended conjugation, facilitating ROS generation and leading to a bathochromic-shift absorption and emission. Thus, MeOTTMN is expected as an ideal choice for long-wavelength fluorescence imaging-guided PDT. MeOTTMN can be obtained through a facile two-step synthetic protocol as shown in Figure S1, and the structure of it was characterized by ^1H nuclear magnetic resonance spectroscopy (NMR) spectrum, ^{13}C NMR spectrum, and high-resolution mass spectrometry spectrum (Figures S2–S4).

The photophysical properties of MeOTTMN were investigated with ultraviolet-visible (UV-vis) absorption and fluorescence spectrometry. As shown in Figure 1A, a distinct absorption peak at 506 nm and a fluorescence peak at 700 nm of MeOTTMN were observed, implying a good potential for bioimaging. Then, the AIE tendency of MeOTTMN was confirmed using a tetrahydrofuran (THF)/water solvent system (Figures 1B and S5), showing highly boosted fluorescence emission starting from 70% f_{water}. It is believed that the twisted conformation of the MeOTPA moiety is crucial for inhibiting intermolecular π-π stacking, thus contributing to a distinct AIE tendency. Furthermore, to adapt to the physiobiological environment, MeOTTMN was formulated into NPs (MTD) using amphiphilic polymer DSPE-PEG2000. The average hydrodynamic size of the NPs is about 113 nm, measured by dynamic light scattering (DLS) (Figure 1C), slightly larger than that (~107 nm) observed from the transmission electron microscope (TEM) images (Figure S6). Next, the optical properties of NPs were further examined. As shown in Figure 1D, MTD exhibits an absorption peak at 513 nm and an emission peak at 719 nm. Thus, the nanoformulation process barely affected the peak values of the absorption and fluorescence spectrum of MTD. Moreover, the stability of MTD was investigated in pure water, PBS, and Dulbecco's modified Eagle medium (DMEM). As shown in Figures S7 and S8, within a prolonged period of 15 days, either the hydrodynamic size or optical properties of MTD have not changed significantly. However, it still can be noticed that the size of MTD increased over time. Simultaneously, the intensities of the absorption and fluorescence spectra of MTD slightly decreased. We hypothesize that MTD may gradually aggregate to reduce its surface energy, resulting in a slightly larger size and weakened optical properties. Notably, these phenomena were more pronounced when MTD was stored in DMEM. It is believed that DMEM contains complex components, such as amino acids, vitamins, and other nutrients, which may interact with the NPs through noncovalent bonding, leading to further aggregation or structural damage to MTD. Such physical changes in MTD could result in more significant variations in size and optical parameters.

To gain an in-depth expectation into the photophysical behaviors of MeOTTMN, density functional theory (DFT) and time-dependent density functional theory (TD-DFT) are carried out to study the electron orbitals and the transition properties of the molecule. As shown in Figure S9, the highest occupied molecular orbital (HOMO) is predominantly localized on the methoxy-modified TPA unit while the lowest unoccupied molecular orbital (LUMO) is distributed mainly on malononitrile, showing the full separation of electrons and the strong intramolecular charge transfer (ICT) effect. In addition, according to the natural transition orbital (NTO) analyses (Figure 1E), effective mixing of the wave functions between the lowest singlet charge transfer state (^1CT) and the local triplet excited state (^3LE) has been observed. Such dense energy level distributions are highly beneficial for the efficient generation of triplet excitons. The spin-orbit coupling value of MeOTTMN is calculated to be 0.219 cm^{-1}, suggesting a good tendency to generate triplet excitons. In addition, the ΔE_{ST} of MeOTTMN is calculated, revealing an ultrasmall 0.07 eV energy gap for efficient ROS generation (Figure 1F).

Encouraged by the calculation results, the ROS production of MeOTTMN was then evaluated using various fluorescence

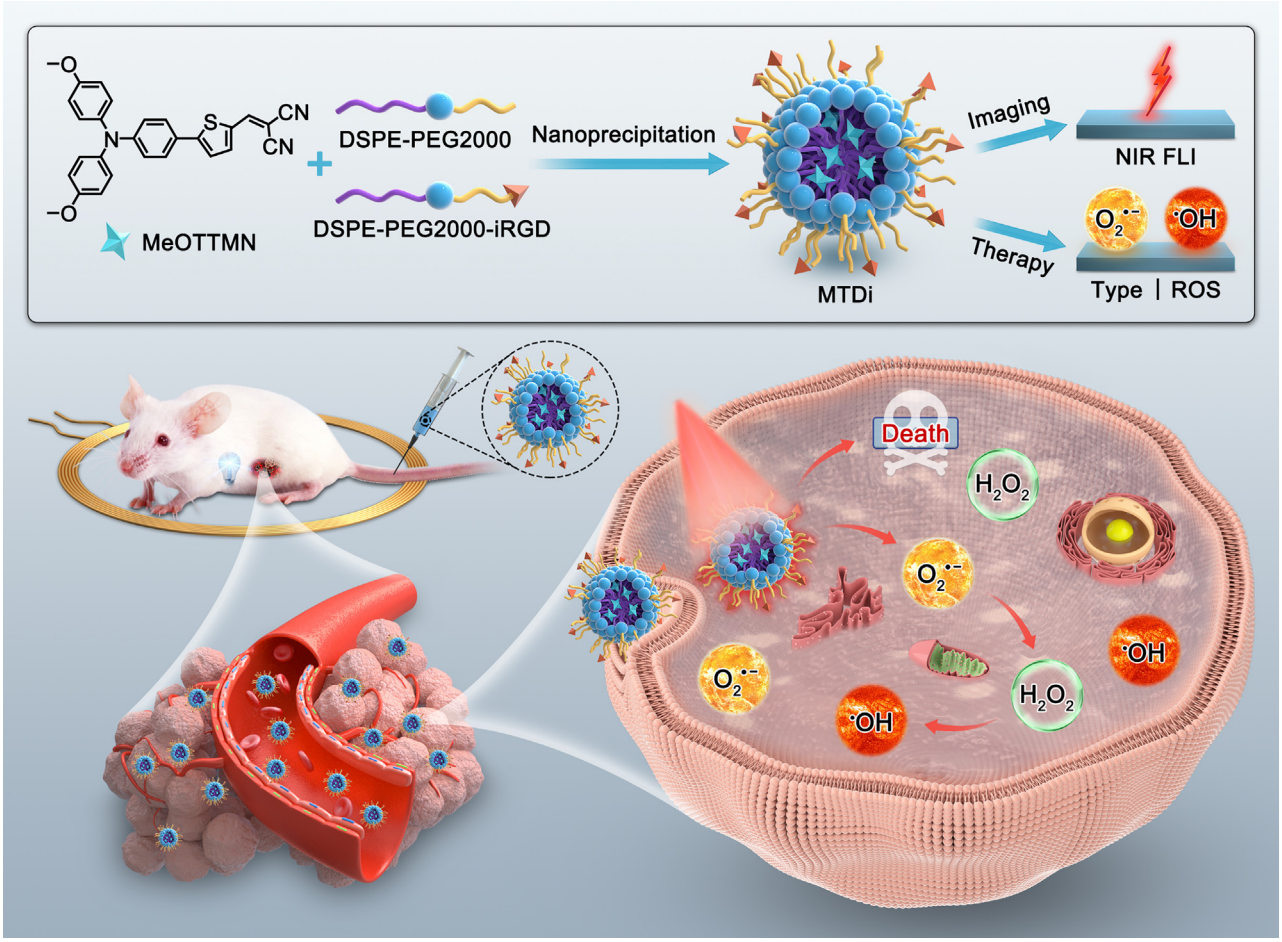

Scheme 1. Schematic illustration of the formulation of MTDi and its type I PDT activated by wireless charging

probes. As shown in Figure S10, the fluorescence intensities of 2′,7′-dichlorodihydrofluorescein (DCFH), the indicator of overall ROS, increase significantly during irradiation in the presence of MTD, much stronger than that enabled by commercial PSs (chlorin e6 [Ce6]). To examine the ROS type generated by MTD, hydroxyphenyl fluorescein (HPF) and dihydrorhodamine 123 (DHR123) were used as indicators for type I ROS ($^{\cdot}OH$ and $O_2^{\cdot-}$) and 9,10-anthracenediyl-bis(methylene)dimalonic acid (ABDA) was used for type II ROS ($^1O_2$) detection, respectively. As demonstrated in Figures S11, S12, and 1G, MTD triggered massive production of $O_2^{\cdot-}$ and $^{\cdot}OH$ compared to Ce6. By contrast, ABDA was barely degraded by MTD within continuous irradiation of 20 min (Figure S13). In addition, electron spin resonance spectroscopy was applied to examine the types of ROS. As shown in Figure S14, weak signal peaks of $^1O_2$ are observed, in sharp contrast to the evident signals of type I ROS. The aforementioned results demonstrated the type I nature of MeOTTMN, which can overcome the therapeutic hurdles in the hypoxic tumor environment.

Since the electron transfer mechanism is the basic principle for type I ROS generation, electrostatic potential (ESP) mapping is performed to study the charge density distribution along the molecular backbone of MeOTTMN. As shown in Figure 1H, the negatively charged domain is primarily distributed in the cyano groups. Therefore, the C≡N bond is considered the active site for one-electron reduction with the production of intermediate radial anion ($MeOTTMN^{\cdot-}$), which can further transfer one electron to triplet oxygen to generate $O_2^{\cdot-}$. The Gibbs free energy changes (ΔG) of this electron transfer process were further calculated to validate its feasibility. In brief, the ΔG of −69.525 kcal/mol has been calculated in the initial one-electron reduction step, indicating a spontaneous reaction. Additionally, the ΔG of the overall electron transfer process to $^3O_2$ with the generation of $O_2^{\cdot-}$ was calculated to be −20.156 kcal/mol, validating the feasibility of type I ROS generation. Thus, it is reasonable to perceive that the generation of type I ROS enabled by MeOTTMN followed by the previously reported mechanism, in which the triplet MeOTTMN firstly captures one electron from hydroxyl anion and then transfers one electron to $^3O_2$, with the generation of $O_2^{\cdot-}$, which further convert to $^{\cdot}OH$ through secondary reactions.

wLED-mediated photodynamic effect

To optimize the photodynamic effect, it is necessary to choose a suitable wLED and understand its physical properties under

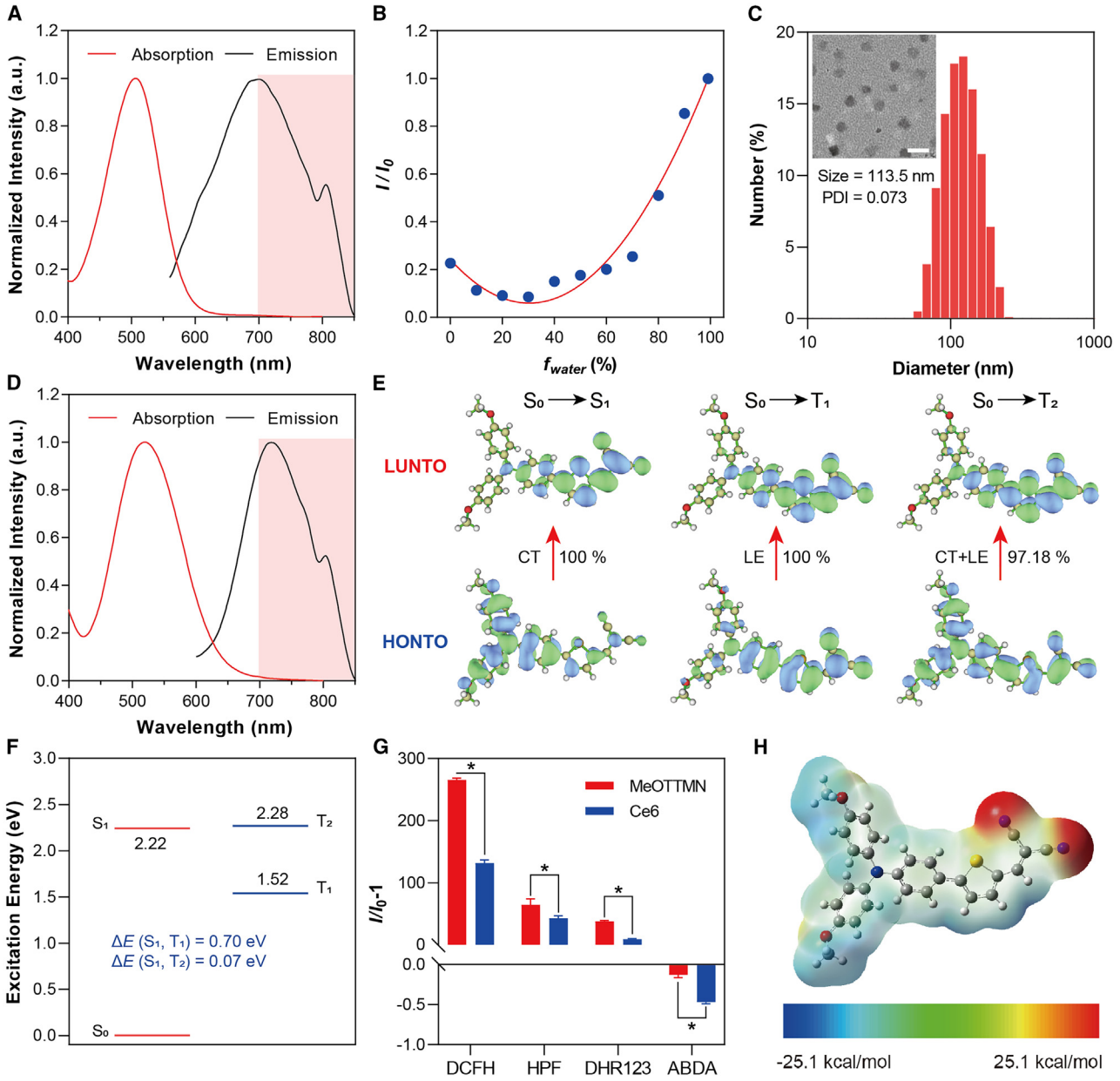

Figure 1. Characterizations of MeOTTMN

(A) Absorption and emission spectra of MeOTTMN in THF.

(B) AIE curve of MeOTTMN.

(C) DLS result and TEM image of MTD (scale bar: 200 nm).

(D) Absorption and emission spectra of MTD.

(E) NTO transition orbitals of MeOTTMN.

(F) The calculated ΔE_{ST} of MeOTTMN.

(G) Photodynamic effect of MTD.

(H) ESP mapping of MeOTTMN. Data are represented as mean ± SEM. One-way ANOVA and two-way ANOVA analysis of variance test was used, followed by Bonferroni multi-comparisons. A p value less than 0.05 was considered to be statistically significant.

wireless charging. Herein, the wLED was composed of a diode and a wireless charging coil and then encapsulated in the waterproof polydimethylsiloxane (Figure S15). To choose a suitable wavelength of wLED for light excitation of MeOTTMN, wLEDs with different emission colors, including blue, green, orange, red, and white, were prepared. As shown in Figure 2A, the emission spectra of wLEDs under wireless charging were presented, which cover the whole range of visible light. The actual photos of

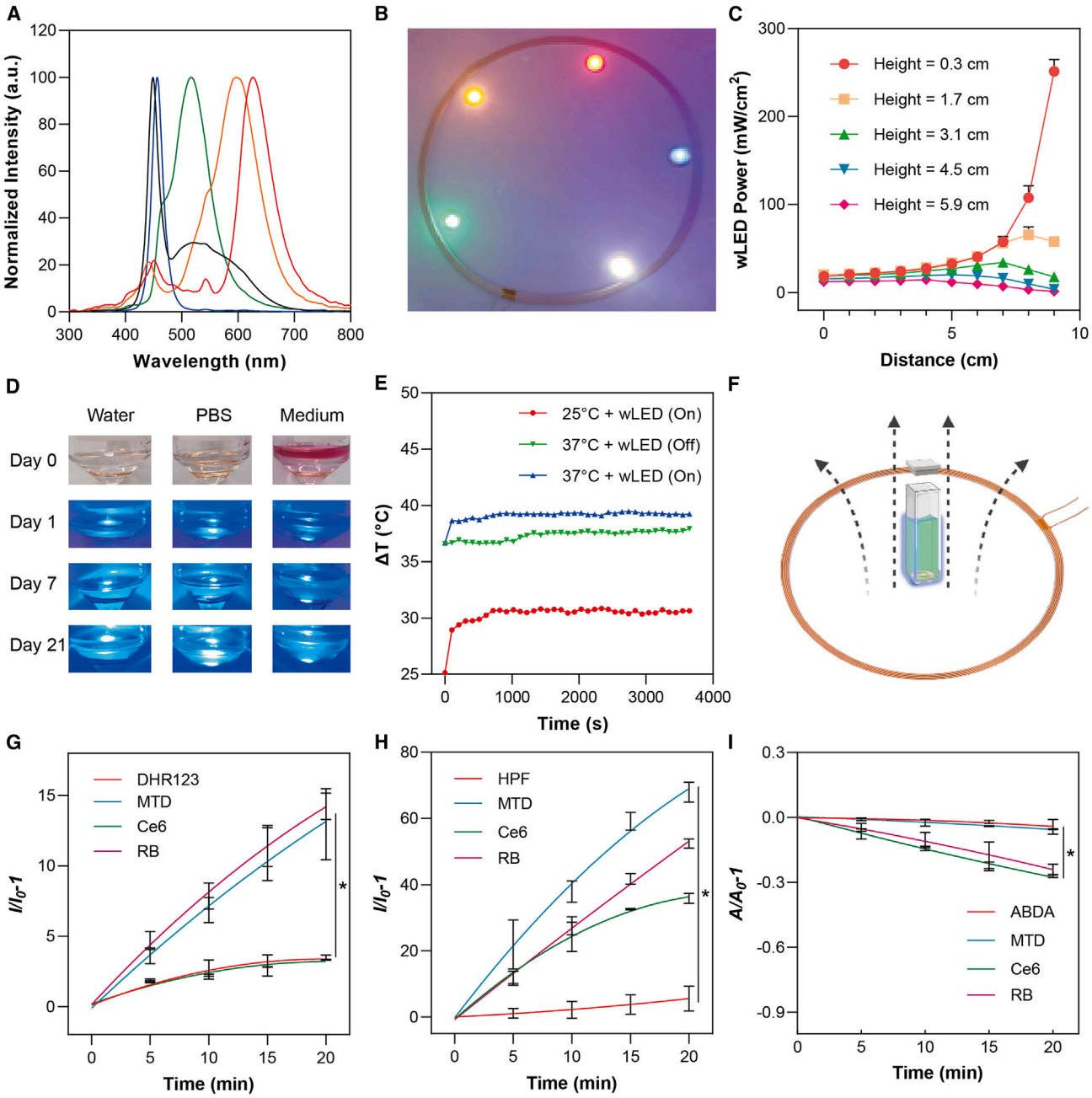

Figure 2. Characterization of the optical properties of the wLED and MTD

(A) Emission spectra of wLEDs with different colors.

(B) Photo of wLEDs lit up through wireless charging.

(C) Output power of blue light emitted wLED at different distances and heights from the center of the wireless charging coil.

(D) Temperature elevation of wLED under different conditions.

(E) wLED soaked in water, PBS, and DFP with wireless charging on day 1, day 7, and day 21.

(F) Schematic illustration of ROS evaluation enabled by wireless charging system.

(G and H) Fluorescence enhancement of (G) DHR123 (for $O_2^{\cdot-}$ detection) and (H) HPF (for $^{\cdot}OH$ detection) in the presence of MTD (2 μM) with wireless charging (output power of wLED: ~19 mW).

(I) Relative decomposition rates of ABDA (for $^1O_2$ detection) in the presence of MTD (2/3 μM) with wireless charging (Output power of wLED: ~19 mW). Data are represented as mean ± SEM. One-way ANOVA and two-way ANOVA analysis of variance test was used, followed by Bonferroni multi-comparisons. A p value less than 0.05 was considered to be statistically significant.

lit-up wLEDs are shown in Figure 2B. It is known that the electrogenerated magnetic field around the wireless charger is unevenly distributed. Thus, it is important to determine the output power of wLED at different relative positions to the charging coil. Blue light-emitting wLEDs are expected to have the strongest photon energy, offering the highest potential to induce an intense photodynamic effect. Therefore, we used blue light-emitting wLEDs to evaluate the photophysical properties of the wLED. As shown in Figure 2C, the output power of a wLED increases as the distance to the coil decreases, due to the greater electromagnetic induction strength near the coil. The maximum power density of the wLED determined by the optical power meter was ~250 mW/cm^2. Next, given the concerns of potential side effects of heat generation, the temperature increment of wLED at 25°C and 37°C ambient temperature was measured by an infrared camera. As shown in Figure 2D, with continuous wireless charging of 10 min, a temperature increase of 5°C was observed starting from 25°C, and a 2.5°C increase was observed starting from 37°C. These results indicate that blue-light emitting wLED has good energy conversion efficiency and does not produce significant thermal effects. Furthermore, the reliability of wLED in the physiological environment was studied. As shown in Figure 2E, wLEDs were soaked in water, PBS, and culture media, respectively, and they could still be lit by wireless charging even after 21 days, laying a solid foundation for long-term *in vivo* biomedical applications.

Next, it is necessary to test and compare the photodynamic performance of MTD with different wLEDs under wireless charging. The measurement setup is shown in Figure 2F. As shown in Figure S16, the blue-light wLED contributed to the strongest ROS production compared to the green-, orange-, and red-light wLED. It is believed that blue light has the highest photon energy that can easily excite electrons from the ground state to the singlet state, leading to stronger ROS production. The ROS production of MTD was further compared with the Ce6 and rose bengal (RB) by adopting an ROS indicator DCFH, DHR123, and HPF. As shown in Figures S17, 2G, and 2H, along with the continuous irradiation, the fluorescence intensity of DCFH, DHR123, and HPF enhanced rapidly in the presence of MTD, faster than that of Ce6 and RB, while negligible fluorescence increase was detected with the ROS indicator alone. In addition, as shown in Figure 2I, negligible decomposition of ABDA has been observed in the presence of MTD, in sharp contrast to the Ce6 and RB groups. Overall, MTD exhibited a similar trend of ROS production under wireless charging compared to conventional measurement methods regarding intensities and type. In addition, due to the simple setup of this wireless charging system, two charging coils have been used to evaluate the photodynamic effect of MTD. However, as shown in Figure S18, within a continuous wireless charging period, a negligible difference was observed between MTD activated by one and two coils. Thus, one charging coil was used in the following experiments.

wLED-mediated *in vitro* photodynamic therapy

Subsequently, the cellular uptakes of MTD by 4T1 cells were studied after 12 h incubation. It was observed that MTD can easily enter 4T1 cells even with a very low concentration of 0.1 μM (Figure S19). In brief, MTD of 0.1 μM has contributed to a mean fluorescence intensity (MFI) of 8.1×10^5, which is far higher than the MFI of 1.2×10^4 of blank control. The confocal fluorescence images revealed the MTD distribution in the cytoplasm with red fluorescence around the DAPI-stained nucleus (Figure 3A). In addition, a concentration-dependent cellular uptake of MTD has been verified by both confocal fluorescence imaging (Figure S20), indicating an efficient and controllable cellular uptake. The cytotoxicity of MTD at various concentrations was studied on human breast cancer cells (Hs578T and MCF7), cervical cancer cells (HeLa), and mouse breast cancer cells (4T1). As shown in Figure S21, the cell survival rate reached over 85% even at a relatively high concentration of 120 μM after culturing for 24 h, implying the negligible cytotoxicity of MTD.

In light of the good type I ROS production and biocompatibility of MTD, the light-induced tumoricidal activities of MTD toward 4T1 cells were then investigated. Initially, the light-triggered ROS production of MTD inside cells was studied upon exposure to a wLED under wireless charging. The experimental setup was demonstrated in Figure S22. It should be noted that the light power exposed to the cell surface dropped to nearly 4.8 mW according to the relative position between wLED and cells. As shown in Figure S23, with a short irradiation time of 1 min in both normoxic and hypoxic conditions, a distinct green DCFH fluorescence signal was observed in 4T1 cells, revealing an efficient ROS generation by MTD. In contrast, no DCFH signal has been observed in PBS and MTD (without light irradiation) groups. Further, the intracellular ROS generation of MTD under both normoxic and hypoxic conditions was studied (Figure S24). As can be seen in Figure 3B, stronger mean fluorescence intensities (MFIs) have been observed in the hypoxic condition across diverse concentrations. It is believed that hypoxia can modify the activity of the cytochrome chain responsible for mitochondrial oxidative phosphorylation and decrease the activity of the cellular antioxidant system, thereby increasing ROS production and leading to enhanced oxidative stress.[40]

It is worth mentioning that although the power density of wLED light is far inferior to the light source used in the conventional PDT, the irradiation time and frequency can be increased, thereby strengthening the therapeutic effect. Such an assumption was confirmed by the *in vitro* experiments. When the irradiation time was prolonged to 20 min, the therapeutic effect of PDT was hugely improved (Figure S25A). In addition, PDT with two times of irradiation contributed to much better therapeutic effects (Figure S25B) at any concentration of MTD. The *in vitro* PDT was then studied systematically under wireless charging. As shown in Figure 3C, the therapeutic effect of PDT in hypoxic conditions was generally stronger than that in normoxic conditions. Moreover, two irradiations of PDT obviously enlarged the therapeutic effects within any concentrations of MTD. Such phenomenon can be explained by the following reasons: (1) stronger cell damage was induced in the hypoxic condition owing to the disorder of mitochondrial and the cellular antioxidant system; (2) cells cultured in the hypoxic condition may not proliferate as fast as in the normoxic condition; and (3) the increased irradiation time and frequency could induce more oxidative stress. Remarkably, only 12% of cells survived after the wireless PDT mediated even by 10 μM of MTD in hypoxic conditions. Such performance

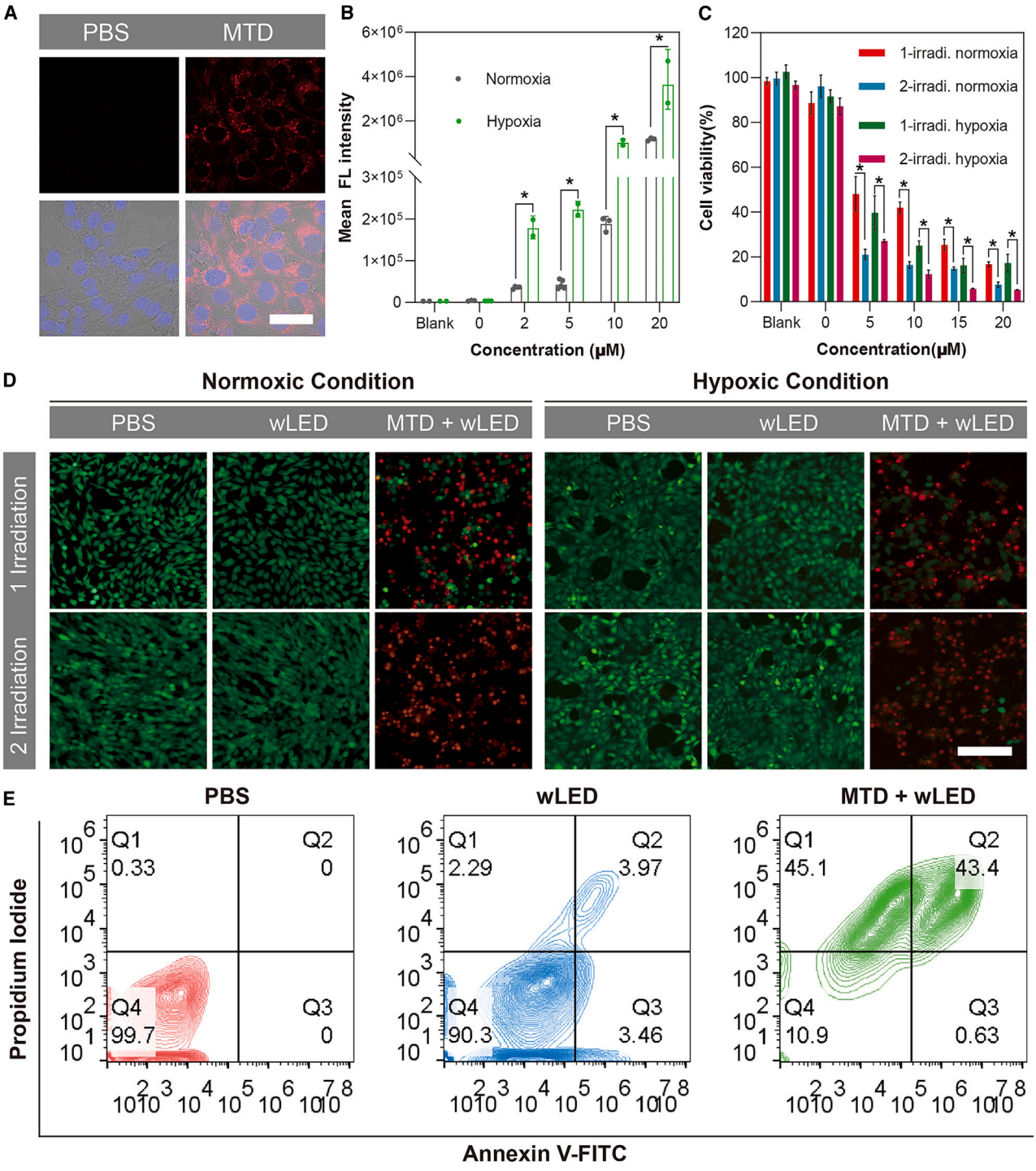

Figure 3. *In vitro* experiments using MTD

(A) Confocal images of 4T1 cells incubated with MTD for 12 h. Blue: DAPI, red: fluorescence signal of MTD (scale bar: 20 μm).

(B) Intracellular ROS production of MTD with different concentrations in normoxic and hypoxic conditions quantified by flow cytometry.

(C) Efficacy of *in vitro* wireless PDT of MTD with different concentrations in normoxic and hypoxic conditions.

(D) Live/dead cell analysis of MTD to 4T1 cells with PI (red) and calcein-AM (green) staining in normoxic and hypoxic conditions (scale bar: 100 μm).

(E) Apoptosis and necrosis analysis of 4T1 cells treated with MTD-mediated PDT in hypoxic conditions by flow cytometry. Data are represented as mean ± SEM. One-way ANOVA and two-way ANOVA analysis of variance test was used, followed by Bonferroni multi-comparisons. A p value less than 0.05 was considered to be statistically significant.

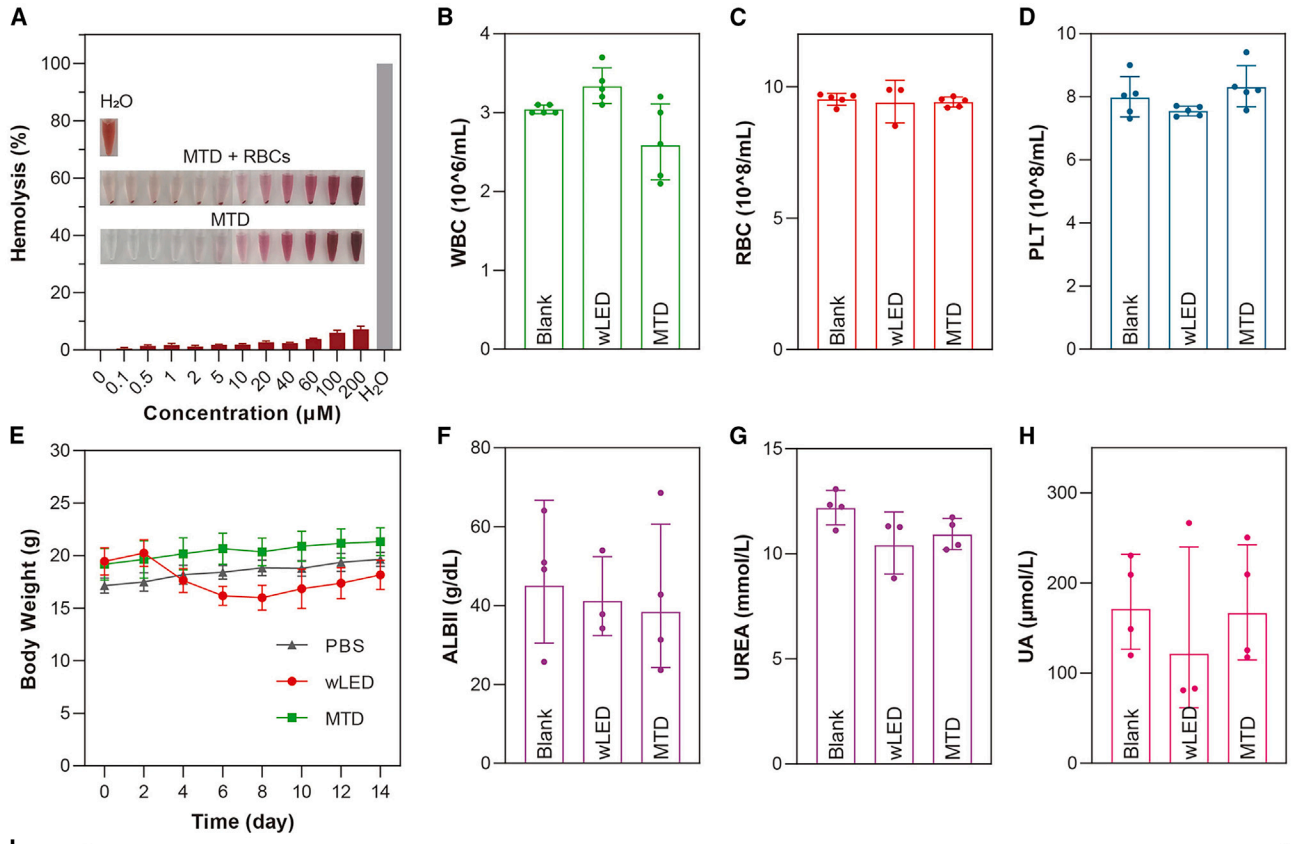

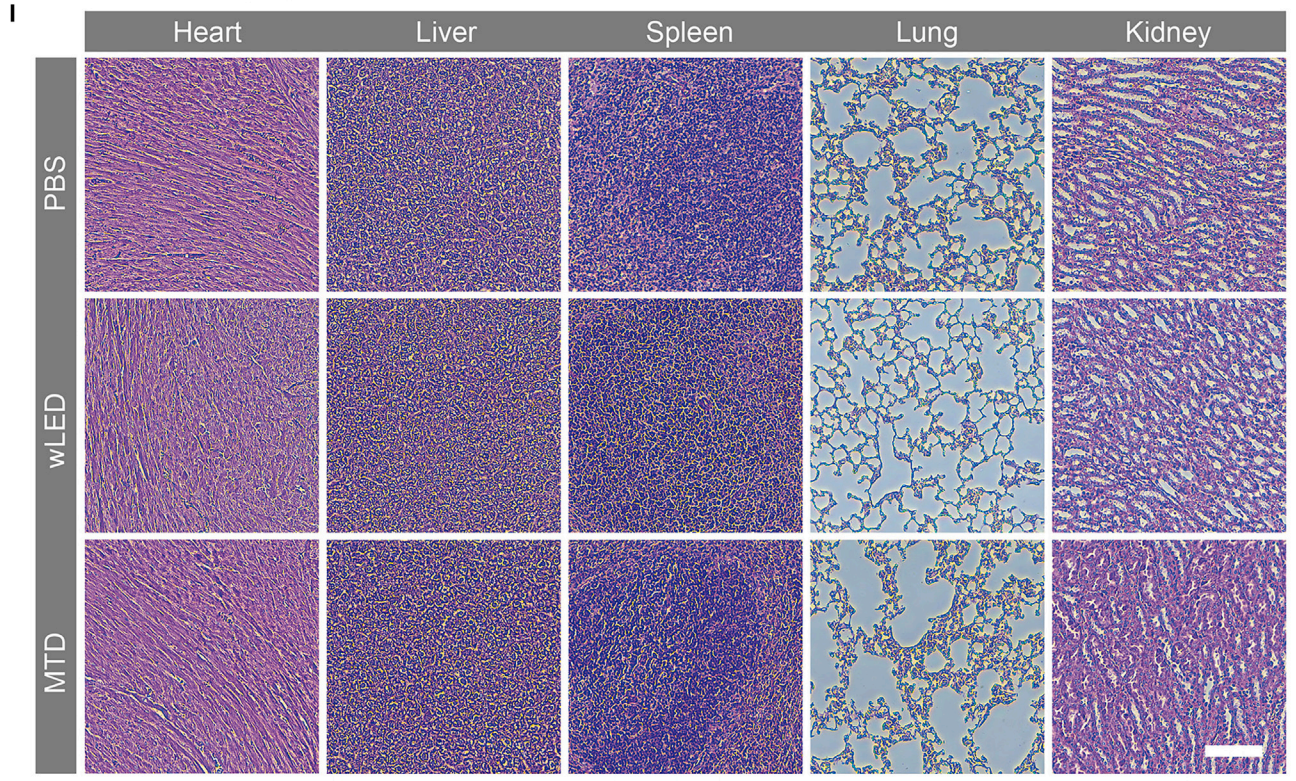

(legend on next page)

was comparable to or even better than the results acquired by the conventional PDT. The therapeutic outcomes were also demonstrated by a bright field microscope. As shown in Figure S26, cells lost their morphology in both normoxic and hypoxic conditions after the photodynamic treatment enabled by wireless charging. Furthermore, a live/dead cell staining assay was performed to assess the efficacy of wireless PDT. As shown in Figure 3D, red fluorescence from PI was dominated in the group treated with MTD + wLED, meanwhile no dead cells were observed without the presence of MTD. It can also be seen that cells cultured in the normoxic condition grew more evenly with higher cell density at the second irradiation time. Such a phenomenon was well matched with the previous results and consumptions. Flow cytometry assay was further used to study the apoptosis of 4T1 cells after the treatment of MTD under normoxic (Figure S27) and hypoxic (Figure 3E) conditions. After ROS generation from MTD to 4T1 cells, the ratio of cell apoptosis and necrosis increased to 85.8% in normoxic conditions and 88.5% in hypoxic conditions, reconfirming the *in vitro* cell death caused by type I ROS. Furthermore, the MTD-treated 4T1 cells were also observed under a fluorescence microscope. The results clearly indicate the apoptosis mechanism of MTD-mediated PDT (Figure S28).

Assessment of the safe use of wLED and MTD

Considering the significance of safety in cancer treatment, the biocompatibility and potential bio-toxicity of wLED and MTD were systematically evaluated by hemolysis, weight recording, blood biochemistry test, blood routine test, and histological analysis. As shown in Figure 4A, MTD did not induce significant rupture of red blood cells (RBCs) even at a high concentration of 200 μM, indicating the bio-inertness of MTD when circulating in the blood system. This feature is expected to maintain a longer circulation time for MTD than for pure MeOTTMN inside the body and help to ensure the accumulation of MTD in the tumor site. To perform an *in vivo* wireless PDT, a wLED diode needed to be implanted inside the body. It is important to know the physiological conditions of mice. Thus, the mice's body weight was recorded every two days after the implantation surgery. As shown in Figure 4E, in the wLED-implanted group, the body weight was slightly decreased in the first 6 days and then bounced back to a similar value compared to the control groups (blank group and MTD-injected group), implying negligible systemic side effects of the implantation surgery. The mouse implanted with wLED behaved normally, and the wLED functioned normally under wireless charging (Video S1). On day 15, all mice were sacrificed, and blood and organs were collected for further analysis. As shown in Figures 4B–4D, three major indexes of blood routine tests, including the number of white blood cell (WBC), RBC, and platelet (PLT), remained nearly unchanged among blank, wLED, and MTD groups, indicating no inflammation has been observed. Moreover, 12 advanced and subdivided indexes of blood routine tests did not reveal significant differences among these three groups (Figure S29). The organ functions of mice were studied by the blood biochemistry test. As shown in Figures 4F–4H, albumin (ALBII), blood urea nitrogen (UREA), and uric acid (UA) stayed in the healthy range for kidney functions. Additional indexes in Figure S30 did not reveal any abnormal issues in liver and kidney functions. Histological analysis of five major organs, including the heart, liver, spleen, lung, and kidney, from the blank, wLED-implanted, and MTD-injected groups were then carefully evaluated. As shown in Figure 4I, lymphocyte infiltration and necrosis were absent, and the cell morphologies remained healthy and normal in all organs. In addition, no pulmonary fibrosis has been found in the lung sections. Normal red and white pulp structures can be clearly seen in the spleen sections. Abnormal glomerulus and tubule structures have not been observed in the kidney sections. These results indicated that the implantation of wLED and the injection of MTD have negligible biotoxicity and side effects on mice, laying a solid foundation for *in vivo* wireless PDT.

wLEDs-mediated type I photodynamic therapy

Encouraged by the good *in vitro* therapeutic effect of wLED-triggered MTD-mediated PDT and their limited bio-toxicity, *in vivo* PDT was tested and carried out based on 4T1 tumor-bearing mice. Initially, a mouse was implanted with wLED and 4T1 cells sequentially followed by 12 days of feeding to heal the wound and grow the tumor. Then, the mouse was placed in the charging coil to trigger the wLED for *in vivo* PDT (Figure 5A). As shown in Figure 5B, on day 0, the wound on the abdomen of a mouse was completely closed, and bright blue light appeared under wireless charging. Next, *in vivo* fluorescence imaging was applied to the organs and tumors of mice after the intravenous injection of NPs, in order to determine the most suitable time for PDT. It is worth mentioning that iRGD peptide was attached on the surface of MTD (namely MTDi) to endow with better targeting ability to 4T1 tumor. The characterization results were summarized in Figure S31, indicating the successful preparation of MTDi. Next, as shown in Figure S32, the strongest fluorescence of MTDi in the tumor was realized at 12 h post-injection, suggesting the maximum retention of NPs and the suitable therapeutic time. It can also be observed that MTDi accumulated in the liver and kidney at the first 6 h, followed by gradual decaying. This phenomenon implied that both the liver and urine are major clearance routes to MTDi.[41,42] The accumulation in the lung was believed to be related to the size effect of MTDi and the rich vascular system in the lung.

Figure 4. Safety assessment of wLED and MTD

(A) Hemolysis rate of MTD at different concentrations.

(B–D) Blood routine results of untreated mice (blank), mice implanted with wLED, and mice treated with MTD (10 mg/kg) ($n = 5$). Abbreviations: WBC, white blood cell; RBC, red blood cell; PLT, platelet.

(E) Body weight recording of blank, mice implanted with wLED and mice treated with MTD (10 mg/kg) ($n = 5$).

(F–H) Blood biochemistry of blank, mice implanted with wLED and mice treated with MTD (10 mg/kg) ($n = 5$). Abbreviations: ALBII, albumin; UREA, blood urea nitrogen; UA, uric acid.

(I) Histological images of the major organs of mice at the end of 15 days after treatments (scale bar: 100 μm). Data are represented as mean ± SEM.

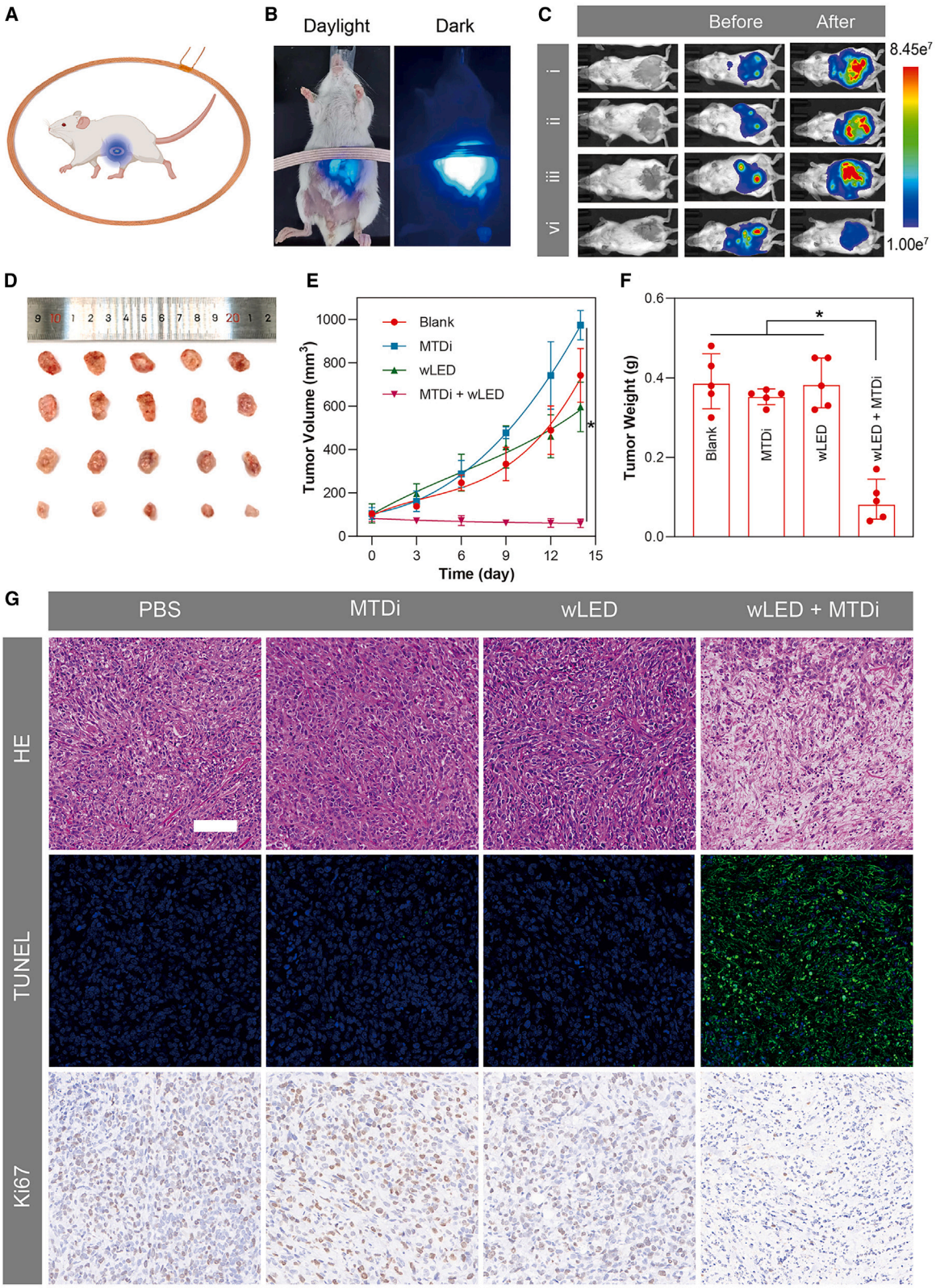

(legend on next page)

To facilitate observation of the growth of the 4T1 tumor, luciferase-expressed 4T1 cells (4T1-luc) were engineered and injected subcutaneously at the abdomen region of the mouse. Bioluminescence can be used to reflect the growth situation of 4T1 cells before and after the overall PDT treatment sessions. As shown in Figure 5C, significant cancer growth can be observed in blank, MTDi, and wLED groups, suggesting no effective therapy has been exerted. In sharp contrast, the region and intensity of bioluminescence were largely reduced in the group of wLED + MTDi attributed to the production of type I ROS. However, considering the high frequency of PDT in the overall treatment session, the bioluminescence indication method, which requires the injection of luciferase substrate, may not be an ideal choice to monitor the growth of the 4T1 tumor. Therefore, the tumor growth was recorded according to the size measured by a vernier caliper. On day 14, all the tumors of each group were collected and displayed in Figure 5D. The result indicated that the combination of wLED and MTDi contributed to a highly efficient therapeutic effect on 4T1 tumors. The tumor growth curves in Figure 5E showed that the tumor volumes in the control groups (blank, wLED, and MTDi-injected) increased sharply during the treatment period and no significant difference was observed among them. Remarkably, upon the introduction of wireless charging, MTDi exhibited an obvious inhibition effect on tumor growth. In addition, the weight of tumors implied a strong therapeutic effect of MTDi-mediated PDT on the tumor-bearing mice, with a tumor inhibition rate of 76.4% (Figure 5F).

During the whole therapeutic session, the body weight of mice in all groups was recorded and summarized in Figure S33. In brief, mice in the blank and MTDi-injected groups exhibited a relatively stable growth curve. In comparison, wLED and wLED + MTDi groups have a sudden drop in weight in the first few days followed by a steady recovery. It is believed that the weight loss was attributed to the postoperative weakness of mice. At the end of the treatment session, the organs and blood of the mice were collected for further analysis. As shown in Figure S34, the organ coefficient among all groups was nearly the same, suggesting there is no severe toxicity of MTDi. In addition, the blood routine and blood biochemistry tests were also performed. As shown in Figures S35 and S36, all the blood indexes appeared normal without significant differences compared to the control groups, indicating the safety of the therapeutic strategy. Additionally, tumor sections from different groups were stained by hematoxylin and eosin (H&E). As shown in Figure 5G, massive nucleus absence and conspicuous karyopyknosis have only been observed on the tumor section treated by wLED + MTDi, suggesting successful destruction of tumor tissue by PDT. In addition, terminal-deoxynucleotidyl transferase-mediated nick end labeling (TUNEL) staining assay was further used to verify the cell apoptosis in tumor tissue induced by MTDi-mediated PDT. Remarkably, a large amount of TUNEL-positive green fluorescence signals was observed on tumor tissue treated with PDT while no green fluorescence signals have been detected in the control groups, implying the severe cell apoptosis induced by PDT. The therapeutic mechanism was further investigated by the monoclonal antibody Ki67 immunofluorescence staining assay. As can be seen in Figure 5G, Ki67-positive proliferating cells were absent in the wLED + MTDi group. In sharp contrast, densely arranged 4T1 cells with strong proliferation activity have been observed in the tumor tissues of control groups. These results convincingly demonstrated that type I PDT enabled by MTDi under wireless charging could effectively inhibit tumor growth by inducing tumor cell apoptosis and suppressing tumor cell proliferation.

Combining type I PDT with a wirelessly powered implanted light source theoretically addresses two major challenges of phototherapy: the penetration depth of the excitation light and the hypoxic environment within tumors. However, for clinical application, the current setup still has significant limitations. On one hand, although the wLED can bypass the barrier posed by skin and adipose tissue, the light's penetration depth within the body remains limited. Therefore, future development still requires the development of PSs that can be excited by long wavelengths, especially in the region of NIR-II window, to further expand the treatment scope. On the other hand, while this work demonstrates *in vivo* treatment conceptually, achieving an efficient therapeutic strategy relies on real-time feedback on treatment outcomes. We need to deliver the therapeutic energy to the lesion precisely to achieve curing effects while providing real-time feedback to avoid over-treatment of healthy tissue. This likely demands greater innovation and advancement in device technology. In short, the future development direction will inevitably involve the strong integration of PSs and electronic devices, necessitating collaborative efforts from researchers.

Conclusion

In this work, we present an innovative therapeutic approach that combines type I AIE PS, MeOTTMN, with a wireless charging system to suppress tumor growth remotely and on demand. The implantable wLED offers the possibility of exciting PS via internal excitation inside the body, thereby overcoming the limitations of light penetration. In addition, by encapsulating the wLED in a biocompatible and nondegradable material, we ensure its long-term retention in the body for sustained photodynamic

Figure 5. *In vivo* PDT mediated by MTDi under wireless charging

(A) Schematic illustration of *in vivo* PDT under wireless charging.

(B) Photos of a mouse under daylight and dark conditions under wireless charging.

(C) Bioluminescence of mice in different groups before and after PDT treatment.

(D) Dissected tumors of mice in different groups on day 14.

(E) Tumor growth curves of 4T1-tumor bearing mice with different treatments in a continuous 14 days.

(F) Tumor weight of the dissected tumors of mice in different groups.

(G) H&E, TUNEL, and Ki67 staining of tumor tissues after different treatments (scale bar: 100 μm). Data are represented as mean ± SEM. One-way ANOVA and two-way ANOVA analysis of variance test was used, followed by Bonferroni multi-comparisons. A p value less than 0.05 was considered to be statistically significant.

cancer therapy. To tackle the hypoxic condition of tumors, iRGD-decorated MeOTTMN NPs were employed to target the 4T1 tumor and generated massive type I ROS *in situ*. Both *in vitro* and *in vivo* experimental results robustly demonstrated the therapeutic effect of the proposed wireless PDT strategy. Remarkably, a tumor inhibition rate of 76.4% was realized after the treatment by a wireless-charging wLED. Overall, this research provides a new perspective on photodynamic anti-cancer therapy by overcoming the key limitations of light penetration depth and the need for oxygen consumption.

Limitations of the study

Although this work offers a promising solution to overcome conventional challenges in PDT, such as light blockage by surface tissue and hypoxic conditions at the tumor site, the treatment area is still affected by the wavelength of light emitted from the wLED (although the light is generated inside the body) and the distribution of PSs. Therefore, in future research, we aim to enhance our drug-device combination strategy by incorporating long-wavelength wLEDs, long-wavelength activated PSs, and PSs with improved distribution within the tumor.

RESOURCE AVAILABILITY

Lead contact

The relevant experimental reagents, experimental methods, and related data of this study can be obtained by contacting Zhourui Xu (xuzhouray@szu.edu.cn).

Materials availability

This study did not generate new unique reagents.

Data and code availability

- All data reported in this paper will be shared by the lead contact upon request.
- This paper does not report original code.
- Any additional information required to reanalyze the data reported in this paper is available from the lead contact upon request.

ACKNOWLEDGMENTS

This work was financially supported by the National Natural Science Foundation of China (62205216 and 82201851), GuangDong Basic and Applied Basic Research Foundation (2025A1515010016, 2025A1515011418) Shenzhen Medical Research Fund (A2403014 and D2401012), Shenzhen Science and Technology Program (RCYX20210609104608036), Basic Research Foundation of Shenzhen (JCYJ20240813143321028), Shenzhen Key Medical Discipline Construction Fund (grant no. SZXK028), Shenzhen Basic Science Research (Key Program) (JCYJ20220818095612027), and Medical-Engineering Interdisciplinary Research Foundation of Shenzhen University (2024YG009). The authors also thank the Instrument Analysis Center of Shenzhen University for the equipment used. All animal operations complied with the regulations of the Animal Ethical and Welfare Committee of Shenzhen University (AEWC-SZU). Ethical approval was granted by the Ethics Committee of Shenzhen University (AEWC-202300019).

AUTHOR CONTRIBUTIONS

Conceptualization, Z.X., Xiaoyan Chen, and C.Y.; methodology, S.T., C.Y., Y.L, Xiaoyan Chen, Q.L., M.F., and W.Z.; investigation, S.T., Q.L., M.F., C.Y, and Z.X.; analysis, S.T., Q.L., M.F., Xin Chen, G.X., Xiaoyan Chen, C.Y, and Z.X.; funding acquisition, Xin Chen, Xiaoyan Chen, G.X., and Z.X.; project administration, C.Y., Xiaoyan Chen, and Z.X.; writing – original draft, C.Y., S.T., and Z.X.; writing – review & editing, C.Y., S.T., Xiaoyan Chen, and Z.X.

DECLARATION OF INTERESTS

The authors declare no competing interests.

STAR★METHODS

Detailed methods are provided in the online version of this paper and include the following:

- KEY RESOURCES TABLE
- EXPERIMENTAL MODEL AND STUDY PARTICIPANT DETAILS
  - Cell culture
  - *In vivo* PDT enabled by wireless charging
- METHOD DETAILS
  - Instruments
  - Synthesis of MeOTTMN
  - Preparation of LED
  - Characterization of LED
  - Characterization of MTD
  - Measurement of ROS production
  - Cytotoxicity measurements
  - *In vitro* ROS generation measurements of MTD
  - Live/dead cell staining assay
- QUANTIFICATION AND STATISTICAL ANALYSIS

SUPPLEMENTAL INFORMATION

Supplemental information can be found online at https://doi.org/10.1016/j.isci.2025.112196.

Received: January 12, 2025
Revised: February 9, 2025
Accepted: March 6, 2025
Published: March 11, 2025

REFERENCES

1. Li, X., Lovell, J.F., Yoon, J., and Chen, X. (2020). Clinical development and potential of photothermal and photodynamic therapies for cancer. Nat. Rev. Clin. Oncol. *17*, 657–674. https://doi.org/10.1038/s41571-020-0410-2.
2. Agostinis, P., Berg, K., Cengel, K.A., Foster, T.H., Girotti, A.W., Gollnick, S.O., Hahn, S.M., Hamblin, M.R., Juzeniene, A., Kessel, D., et al. (2011). Photodynamic therapy of cancer: An update. CA Cancer J. Clin. *61*, 250–281. https://doi.org/10.3322/caac.20114.
3. Fan, M., Feng, G., Xia, L., Zhang, Y., Liu, M., Li, Z., Jiang, Y., Yang, C., Law, W.C., Yong, K.T., et al. (2023). Controlling the Energy Relaxation: Organic Doping in AIEgenNanoparticles for Highly Enhanced Intravital Two-Photon Imaging. Adv. Opt. Mater. *11*, 2300255. https://doi.org/10.1002/adom.202300255.
4. Kang, M., Zhang, Z., Xu, W., Wen, H., Zhu, W., Wu, Q., Wu, H., Gong, J., Wang, Z., Wang, D., and Tang, B.Z. (2021). Good Steel Used in the Blade: Well-Tailored Type-I Photosensitizers with Aggregation-Induced Emission Characteristics for Precise Nuclear Targeting Photodynamic Therapy. Adv. Sci. *8*, 2100524. https://doi.org/10.1002/advs.202100524.
5. Pallavi, P., Harini, K., Crowder, S., Ghosh, D., Gowtham, P., Girigoswami, K., and Girigoswami, A. (2023). Rhodamine-Conjugated Anti-Stokes Gold Nanoparticles with Higher ROS Quantum Yield as Theranostic Probe to Arrest Cancer and MDR Bacteria. Appl. Biochem. Biotechnol. *195*, 6979–6993. https://doi.org/10.1007/s12010-023-04475-0.
6. Pallavi, P., Harini, K., Anand Arumugam, V., Gowtham, P., Girigoswami, K., Muthukrishnan, S., and Girigoswami, A. (2022). Nanoformulation of Tetrapyrroles Derivatives in Photodynamic Therapy: A Focus on

Bacteriochlorin. Evid. Based. Complement. Alternat. Med. *2022*, 3011918. https://doi.org/10.1155/2022/3011918.

7. Huang, Z. (2005). A review of progress in clinical photodynamic therapy. Technol. Cancer Res. Treat. *4*, 283–293. https://doi.org/10.1177/153303460500400308.
8. Van Straten, D., Mashayekhi, V., De Bruijn, H.S., Oliveira, S., and Robinson, D.J. (2017). Oncologic Photodynamic Therapy: Basic Principles, Current Clinical Status and Future Directions. Cancers *9*, 19. https://doi.org/10.3390/cancers9020019.
9. Dolmans, D.E.J.G.J., Fukumura, D., and Jain, R.K. (2003). Photodynamic therapy for cancer. Nat. Rev. Cancer *3*, 380–387. https://doi.org/10.1038/nrc1071.
10. Kim, M.M., and Darafsheh, A. (2020). Light sources and dosimetry techniques for photodynamic therapy. Photochem. Photobiol. *96*, 280–294. https://doi.org/10.1111/php.13219.
11. Pallavi, P., Harini, K., Elboughdiri, N., Gowtham, P., Girigoswami, K., and Girigoswami, A. (2023). Infections associated with SARS-CoV-2 exploited *via* nanoformulated photodynamic therapy. ADMET and DMPK *11*, 513–531. https://doi.org/10.5599/admet.1883.
12. Thirumalai, A., Girigoswami, K., Pallavi, P., Harini, K., Gowtham, P., and Girigoswami, A. (2023). Cancer therapy with iRGD as a tumor-penetrating peptide. Bull. Cancer *110*, 1288–1300. https://doi.org/10.1016/j.bulcan.2023.08.009.
13. Mallidi, S., Anbil, S., Bulin, A.L., Obaid, G., Ichikawa, M., and Hasan, T. (2016). Beyond the Barriers of Light Penetration: Strategies, Perspectives and Possibilities for Photodynamic Therapy. Theranostics *6*, 2458–2487. https://doi.org/10.7150/thno.16183.
14. Xu, Z., Deng, X., Feng, G., Zhang, W., Zhang, Y., Zhang, W., Fan, M., Hu, M., Yang, C., Ying, M., et al. (2023). Probing the deep brain: Enhanced multi-photon imaging by aggregation-induced emission luminogens *via* nanocrystallization. Chem. Eng. J. *465*, 142850. https://doi.org/10.1016/j.cej.2023.142850.
15. Sheng, Z., Li, Y., Hu, D., Min, T., Gao, D., Ni, J.-S., Zhang, P., Wang, Y., Liu, X., Li, K., et al. (2020). Centimeter-deep NIR-II fluorescence imaging with nontoxic AIE probes in nonhuman primates. Research *2020*, 4074593. https://doi.org/10.34133/2020/4074593.
16. Xu, Z., Jiang, Y., Shen, Y., Tang, L., Hu, Z., Lin, G., Law, W.-C., Ma, M., Dong, B., Yong, K.-T., et al. (2022). A biocompatible photosensitizer with a high intersystem crossing efficiency for precise two-photon photodynamic therapy. Mater. Horiz. *9*, 1283–1292. https://doi.org/10.1039/D1MH01869H.
17. Xu, Z., Jiang, Y., Fan, M., Tang, S., Liu, M., Law, W.-C., Yang, C., Ying, M., Ma, M., Dong, B., et al. (2021). Aggregation-Induced Emission Nanoprobes Working in the NIR-II Region: From Material Design to Fluorescence Imaging and Phototherapy. Adv. Opt. Mater. *9*, 2100859. https://doi.org/10.1002/adom.202100859.
18. Chinna Ayya Swamy, P., Sivaraman, G., Priyanka, R.N., Raja, S.O., Ponnuvel, K., Shanmugpriya, J., and Gulyani, A. (2020). Near Infrared (NIR) absorbing dyes as promising photosensitizer for photo dynamic therapy. Coord. Chem. Rev. *411*, 213233. https://doi.org/10.1016/j.ccr.2020.213233.
19. Wang, R., Li, X., Zhou, L., and Zhang, F. (2014). Epitaxial Seeded Growth of Rare-Earth Nanocrystals with Efficient 800 nm Near-Infrared to 1525 nm Short-Wavelength Infrared Downconversion Photoluminescence for *In Vivo* Bioimaging. Angew. Chem. Int. Ed. *53*, 12086–12090. https://doi.org/10.1002/anie.201407420.
20. Shao, W., Chen, G., Kuzmin, A., Kutscher, H.L., Pliss, A., Ohulchanskyy, T.Y., and Prasad, P.N. (2016). Tunable Narrow Band Emissions from Dye-Sensitized Core/Shell/Shell Nanocrystals in the Second Near-Infrared Biological Window. J. Am. Chem. Soc. *138*, 16192–16195. https://doi.org/10.1021/jacs.6b08973.
21. Yi, H., Ghosh, D., Ham, M.-H., Qi, J., Barone, P.W., Strano, M.S., and Belcher, A.M. (2012). M13 Phage-Functionalized Single-Walled Carbon Nanotubes As Nanoprobes for Second Near-Infrared Window Fluorescence Imaging of Targeted Tumors. Nano Lett. *12*, 1176–1183. https://doi.org/10.1021/nl2031663.
22. Chen, G., Sun, Y., Chen, R.R., Biz, C., Fisher, A.C., Sherburne, M.P., Ager Iii, J.W., Gracia, J., and Xu, Z.J. (2021). A discussion on the possible involvement of singlet oxygen in oxygen electrocatalysis. JPhys Energy *3*, 031004. https://doi.org/10.1088/2515-7655/abe039.
23. Wan, Y., Fu, L.H., Li, C., Lin, J., and Huang, P. (2021). Conquering the hypoxia limitation for photodynamic therapy. Adv. Mater. *33*, 2103978. https://doi.org/10.1002/adma.202103978.
24. Li, M., Xu, Y., Peng, X., and Kim, J.S. (2022). From low to no O_2-dependent hypoxia photodynamic therapy (hPDT): a new perspective. Acc. Chem. Res. *55*, 3253–3264. https://doi.org/10.1021/acs.accounts.2c00531.
25. Manning, E.P. (2016). Central nervous system oxygen toxicity and hyperbaric oxygen seizures. AMHP *87*, 477–486. https://doi.org/10.3357/AMHP.4463.2016.
26. Plafki, C., Peters, P., Almeling, M., Welslau, W., and Busch, R. (2000). Complications and side effects of hyperbaric oxygen therapy. ASEM *71*, 119–124. https://europepmc.org/article/med/10685584.
27. Kim, H.-J., Hirayama, H., Kim, S., Han, K.J., Zhang, R., and Choi, J.-W. (2017). Review of near-field wireless power and communication for biomedical applications. IEEE Access *5*, 21264–21285. https://doi.org/10.1109/ACCESS.2017.2757267.
28. Zhou, Y., Liu, C., and Huang, Y. (2020). Wireless Power Transfer for Implanted Medical Application: A Review. Energies *13*, 2837. https://doi.org/10.3390/en13112837.
29. Bansal, A., Yang, F., Xi, T., Zhang, Y., and Ho, J.S. (2018). *In vivo* wireless photonic photodynamic therapy. Proc. Natl. Acad. Sci. *115*, 1469–1474. https://doi.org/10.1073/pnas.171755211.
30. Yamagishi, K., Kirino, I., Takahashi, I., Amano, H., Takeoka, S., Morimoto, Y., and Fujie, T. (2019). Tissue-adhesive wirelessly powered optoelectronic device for metronomic photodynamic cancer therapy. Nat. Biomed. Eng. *3*, 27–36. https://doi.org/10.1038/s41551-018-0261-7.
31. Arami, H., Kananian, S., Khalifehzadeh, L., Patel, C.B., Chang, E., Tanabe, Y., Zeng, Y., Madsen, S.J., Mandella, M.J., Natarajan, A., et al. (2022). Remotely controlled near-infrared-triggered photothermal treatment of brain tumours in freely behaving mice using gold nanostars. Nat. Nanotechnol. *17*, 1015–1022. https://doi.org/10.1038/s41565-022-01189-y.
32. Wright, J.P., Mughrabi, I.T., Wong, J., Mathew, J., Jayaprakash, N., Crosfield, C., Chang, E.H., Chavan, S.S., Tracey, K.J., Pavlov, V.A., et al. (2022). A fully implantable wireless bidirectional neuromodulation system for mice. Biosens. Bioelectron. *200*, 113886. https://doi.org/10.1016/j.bios.2021.113886.
33. Li, B., Ji, P., Peng, S.Y., Pan, P., Zheng, D.W., Li, C.X., Sun, Y.X., and Zhang, X.Z. (2020). Nitric Oxide Release Device for Remote-Controlled Cancer Therapy by Wireless Charging. Adv. Mater. *32*, 2000376. https://doi.org/10.1002/adma.202000376.
34. Chen, K., He, P., Wang, Z., and Tang, B.Z. (2021). A Feasible Strategy of Fabricating Type I Photosensitizer for Photodynamic Therapy in Cancer Cells and Pathogens. ACS Nano *15*, 7735–7743. https://doi.org/10.1021/acsnano.1c01577.
35. Li, Y., Zhang, D., Yu, Y., Zhang, L., Li, L., Shi, L., Feng, G., and Tang, B.Z. (2023). A Cascade Strategy Boosting Hydroxyl Radical Generation with Aggregation-Induced Emission Photosensitizers-Albumin Complex for Photodynamic Therapy. ACS Nano *17*, 16993–17003. https://doi.org/10.1021/acsnano.3c04256.
36. Zhang, Z., Kang, M., Tan, H., Song, N., Li, M., Xiao, P., Yan, D., Zhang, L., Wang, D., and Tang, B.Z. (2022). The fast-growing field of photo-driven theranostics based on aggregation-induced emission. Chem. Soc. Rev. *51*, 1983–2030. https://doi.org/10.1039/D1CS01138C.
37. Zhang, W., Li, X., Kang, M., Zhang, Z., Pei, Y., Fan, M., Yan, D., Zhang, Y., Yang, C., Xu, G., et al. (2024). Anthraquinone-Centered Type I Photosensitizer with Aggregation-Induced Emission Characteristics for

Tumor-Targeted Two-Photon Photodynamic Therapy. ACS Mater. Lett. *6*, 2174–2185. https://doi.org/10.1021/acsmaterialslett.4c00600.

38. Zhang, J., Mukamel, S., and Jiang, J. (2020). Aggregation-Induced Intersystem Crossing: Rational Design for Phosphorescence Manipulation. J. Phys. Chem. B *124*, 2238–2244. https://doi.org/10.1021/acs.jpcb.0c00654.

39. Wang, D., Su, H., Kwok, R.T.K., Shan, G., Leung, A.C.S., Lee, M.M.S., Sung, H.H.Y., Williams, I.D., Lam, J.W.Y., and Tang, B.Z. (2017). Facile Synthesis of Red/NIR AIE Luminogens with Simple Structures, Bright Emissions, and High Photostabilities, and Their Applications for Specific Imaging of Lipid Droplets and Image-Guided Photodynamic Therapy. Adv. Funct. Mater. *27*, 1704039. https://doi.org/10.1002/adfm.201704039.

40. Coimbra-Costa, D., Alva, N., Duran, M., Carbonell, T., and Rama, R. (2017). Oxidative stress and apoptosis after acute respiratory hypoxia and reoxygenation in rat brain. Redox Biol. *12*, 216–225. https://doi.org/10.1016/j.redox.2017.02.014.

41. Ngo, W., Ahmed, S., Blackadar, C., Bussin, B., Ji, Q., Mladjenovic, S.M., Sepahi, Z., and Chan, W.C.W. (2022). Why nanoparticles prefer liver macrophage cell uptake *in vivo*. Adv. Drug Deliv. Rev. *185*, 114238. https://doi.org/10.1016/j.addr.2022.114238.

42. Cassano, D., Pocoví-Martínez, S., and Voliani, V. (2017). Ultrasmall-in-nano approach: Enabling the translation of metal nanomaterials to clinics. Bioconjug. Chem. *29*, 4–16. https://doi.org/10.1021/acs.bioconjchem.7b00664.

STAR★METHODS

KEY RESOURCES TABLE

REAGENT or RESOURCE	SOURCE	IDENTIFIER
Chemicals, peptides, and recombinant proteins		
Distearoyl-sn-glycero-3-phosphoethanolamine-N-(methoxy-(polyethylene glycol)-2000)	Xi'an ruixi Biological Technology	LP-R4-039; CAS:147867-65-0
iRGD modified Distearoyl-sn-glycero-3-phosphoethanolamine-N-(methoxy-(polyethylene glycol)-2000)	Xi'an ruixi Biological Technology	R-DP-096; CAS: N/A; http://www.xarxbio.com/pro/pro-13145.html
Calcein-AM	Thermo Fisher Scientific	C3100MP; CAS: 148504-34-1
Propidium Iodide	Thermo Fisher Scientific	P1304MP; CAS: 25535-16-4
2′,7′-dichlorodihydrofluorescein diacetate	Sigma-Aldrich	D6883; CAS: 4091-99-0
Hydroxyphenyl Fluorescein	Sigma-Aldrich	H4290; CAS: 359010-69-8
Dihydrorhodamine 123	Thermo Fisher Scientific	D23806; CAS: 109244-58-8
9,10-Anthracenediyl-bis(methylene) dimalonic Acid	Thermo Fisher Scientific	75068; CAS: 307554-62-7
D-luciferin sodium salt	Solarbio	D9390; CAS: 103404-75-7
4-Bromo-N,N-bis(4-methoxyphenyl)aniline	J&K Scientific	OR1011474; CAS: 194416-45-0
5-formylthiophen-2-boronic acid	J&K Scientific	409351; CAS: 4347-33-5
$Pd(dppf)Cl_2$	Sigma-Aldrich	697230; CAS: 72287-26-4
Critical commercial assays		
Annexin V-FITC/PI	Beyotime Biotechnology	C1062S
Cell counting kit-8	Beyotime Biotechnology	C0038
Experimental models: Cell lines		
Breast cancer cell: 4T1 cell	BeNa Culture Collection	BNCC273810
Luciferase-labeled breast cancer cell: 4T1-Luc cell	BeNa Culture Collection	BNCC342440
Cervical cancer cell: HeLa cell	BeNa Culture Collection	BNCC342189
Breast cancer cell: MCF7 cell	BeNa Culture Collection	BNCC100137
human breast cancer cell: Hs578T cell	BeNa Culture Collection	BNCC339562
Experimental models: Organisms/strains		
Balb/C mice	GUANGDONG MEDICAL LABORATORY ANIMAL CENTER	SPF level Balb/C female mice
Software and algorithms		
ImageJ	Open source	N/A
FlowJo	BD Biosciences	https://www.flowjo.com/
GraphPad Prism	GraphPad	https://www.graphpad.com/

EXPERIMENTAL MODEL AND STUDY PARTICIPANT DETAILS

Cell culture

All the cell lines were purchased from BeNa Culture Collection, which are responsible for the authenticity and healthiness of cell lines. 4T1 cells were grown into the glass-bottom dishes using advanced DMEM, supplemented with 10% fetal calf serum (FBS), and 1% Penicillin-Streptomycin Solution (PS) at 37°C in a humidified atmosphere containing 5% CO_2.

To mimic hypoxic conditions in the tumor microenvironment and, therefore, detect the intracellular ROS generation, an AnaeroPack^{TM}-Abnaero Anaerobic Gas Generator was used to create a hypoxic atmosphere in a sealed chamber. 4T1 cells were pre-cultured in the chamber for 12 h at 37°C before the detection of ROS.

In vivo PDT enabled by wireless charging

The experimental protocol of animal experiments was approved by the Institutional Ethical Committee of Animal Experimentation of Shenzhen University (Approval NO. AEWC-202300019). Experiments were carried out strictly according to governmental and international guidelines on animal experimentation. Female Balb/C mice were purchased from the Guangdong Medical Laboratory Animal Center. Mice were used until 7 weeks old. According to the requirements for Biosafety and Animal Ethics, all efforts were made to minimize the number of animals used and their suffering.

Mice were randomly divided into 4 groups with 5 mice in each group. Tumor-bearing mice models were established by injecting 4T1 cells (1×10^6 cells per mouse) into the abdomen region of mice subcutaneously. Then, LEDs were implanted into mice via surgery. When the wound on the abdomen was healed and the tumor volumes reached the size of approximately 50-60 mm^3, mice were ready to receive different treatments. In specific, mice in the blank group were fed without treatment; mice in the MTDi group were injected with each 200 μL MTDi (1 mM) on day 0, 3, 6, and 9, respectively; mice in the LED group were implanted with LEDs without further treatment; mice in the LED + MTDi group was implanted with LEDs and injected with MTDi and performed the PDT under wireless charging. In addition, 1 h of irradiation enabled by wireless charging was performed in each therapeutic session. Tumor length (L: mm) and width (W: mm) were measured every 3 days, and the calculation formula for tumor volume (V) was: V (mm^3) = $0.5 \times L \times W^2$. The body weights of the mice were also recorded and analyzed. Mice were sacrificed after 14 days of treatment. The heart, liver, spleen, lung, kidney, and cancer were collected and analyzed by HE staining. TUNEL assay and Ki67 staining were performed on tumor tissues.

METHOD DETAILS

Instruments

UV-vis and photoluminescence spectra were recorded using TP-720 (Tian Jin Tuo Pu Instruments Co., Ltd) and F-4600 (HITACHI, Ltd) respectively. The morphology and composition of nanoparticles were analyzed by a field emission transmission electron microscope (F200, JEOL Ltd.). Hydrodynamic diameter and polydisperse index were measured by Zetasizer-Nano-ZS90 (Malvern Instruments Ltd.) At room temperature. Fluorescent images of cell samples were captured by fluorescent microscope (EVOS M5000, Invitrogen) and Ultra-high resolution confocal microscope (ZEISS-LSM880).

Synthesis of MeOTTMN

4-Bromo-N,N-bis(4-methoxyphenyl)aniline (192 mg, 0.5 mmol, 1.0 eq), 5-formylthiophen-2-boronic acid (234 mg, 0.75 mmol, 2.0 eq), and K_2CO_3 (345 mg, 2.5 mmol, 5.0 eq) were added in mixed solvent MeOH/Toluene (v/v = 1:1). The $Pd(dppf)Cl_2$ (36 mg, 0.05 mmol, 10 mol%, 0.1 eq) was added into the mixture under N_2 protection. The reaction mixture was heated to 75°C for 16 h. After 16 h, the reaction mixture was filtered, and the solvent was removed. The residue was dissolved in DCM, and Et_3N (10 drops), and malononitrile (60 mg, 1 mmol, 2.0 eq) were added to the above solution. The reaction mixture was stirred under 30°C for 16 h. After 16 h, the reaction mixture was filtered, and the solvent was removed. The residue was purified by silica gel chromatography using Hex/EtOAc (v/v = 3:1) as eluent. MeOTTMN was obtained as black solid in 25% yield. ^{1}H NMR (500 MHz, DMSO-d_6) δ 8.55 (s, 1H), 7.89 (s, 1H), 7.61 (d, J = 9.0 Hz, 3H), 7.12 (d, J = 8.7 Hz, 4H), 6.96 (d, J = 8.8 Hz, 4H), 6.75 (d, J = 8.7 Hz, 2H), 3.76 (s, 6H). ^{13}C NMR (126 MHz, DMSO-d_6) δ 156.62, 156.33, 152.23, 150.33, 142.96, 138.76, 132.40, 127.69, 123.63, 122.39, 117.67, 115.15, 114.24, 72.43, 55.29. HRMS (ESI): m/z calculated for $C_{28}H_{21}N_3O_2S$, [M+H]: 464.1432, found 464.1417.

Preparation of LED

Tin foil was used to make a cylindrical mold with a bottom diameter of 1.2cm and a height of 1cm. Next, the PDMS solution was homogenously mixed with the curing agent at a ratio of 10:1, followed by soaking the LED. After 6 h of incubation at 65°C, a waterproof LED was obtained.

Characterization of LED

LED was lit up by a wireless charging coil. The emission spectra of LED with different colors were measured using a fluorescence spectrophotometer. A power meter (THOR LABS) was used to measure the output power of the LED under the wireless charging coil. A FLIR A300 thermographic camera was used to measure the temperature change of LED during operation.

Characterization of MTD

The size and morphology of the MTD in ultra-pure water were analyzed on a transmission electron microscope (TEM). The concentration of MTD was 50 μM during the TEM analysis. The stability of these NPs in ultrapure water, PBS, and Dulbecco's Modified Eagle Medium (DMEM) was analyzed by dynamic light scattering (DLS) according to the variation of the hydrodynamic size of MTD. The concentration of MTD was 50 μM during the DLS analysis. The absorption and emission spectrum of MTD were measured by UV-vis spectrophotometer and fluorescence spectrophotometer. The concentration of MTD was 50 μM during the TEM analysis with ultrapure water, PBS, and DMEM as solvents. The MTD sample was kept at room temperature throughout all characterizations and during storage.

Measurement of ROS production

The total ROS production of the MTD in PBS was measured using H2DCFDA. In brief, 1 mL 10 mM NaOH and 0.25 mL 1 mM H2DCFDA were mixed in the dark condition for 30 minutes for activation. Then, the solution mentioned above was mixed with 5 mL ice-cold PBS solution to obtain a DCFH working solution. Next, 375 μL DCFH working solution, 6 μL 1 mM MTD and 2619 μL PBS were mixed. The production of total ROS can be measured by monitoring the increase in the fluorescence peak value at 520 nm under excitation at 488 nm at time points of 0, 5, 10, 15, and 20 minutes. The production of Type I ROS was measured using DHR123 (the indicator of $O_2^{\cdot -}$) and HPF (the indicator of $^{\cdot}OH$). PBS containing 5 μM DHR123 or HPF and 2 μM MTD were prepared before characterization. The production of $O_2^{\cdot -}$ can be measured by monitoring the increase in the fluorescence peak value at 524 nm under excitation at 495 nm at time points of 0, 5, 10, 15, and 20 minutes. The production of $^{\cdot}OH$ can be measured by monitoring the increase in the fluorescence peak value at 521 nm under excitation at 490 nm at time points of 0, 5, 10, 15, and 20 minutes. The production of Type II ROS was measured using ABDA as the indicator of $^1O_2$. In brief, 3 μL 20 mM ABDA and 3 μL 2 mM MTD were added into 2994 μL PBS. The production of the $^1O_2$ was measured by recording the absorbance of ABDA at 398 nm at time points of 0, 5, 10, 15, and 20 minutes. Chlorin e6 (Ce6) and rose bengal (RB) were used as reference photosensitizers. The power of the white light source is ~20 mW. During the measurement of ROS, the position of the light source, power settings, irradiation time, and sample concentrations were kept consistent across all tests.

Cytotoxicity measurements

4T1 cells were seeded in a 96-well plate at a density of 1×10^4 cells/well and cultured overnight for adherence. Then cells were incubated with different concentrations of MTD for 24 h, and cell viability was evaluated using the Cell Counting Kit 8 by measuring the OD_{450}. Cell viability was calculated according to the following formula: Cell viability (%) = OD_{450} of the test well/OD_{450} of the control well (Blank group) × 100%.

In vitro ROS generation measurements of MTD

4T1 cells were cultured in a 24-well plate for 24 h. Then, 4T1 cells were incubated with various concentrations of MTD nanoparticles for 12 hours. Then, DCFH-DA (10 μM) was added and stained for 20 min. Next, the 24-well plate was irradiated for 20 min by blue-light LED (~4.8 mW) while control groups were kept in the dark. Flow cytometric analysis was used to measure the fluorescence of DCFH-DA by flow cytometry. Fluorescence images were captured by fluorescent microscope.

Live/dead cell staining assay

Live/dead cell staining assay was performed using Calcein/PI Cell Viability/Cytotoxicity Assay Kit. At first, 4T1 cells were cultured in a 24-well plate for 24 h. Then, MTD of different concentrations was added. After 12h, the 24-well plate was irradiated for 20 min by blue-light LED (~4.8 mW) under wireless charging while control groups were kept in the dark. After 8 h, staining solution (300 μL containing 2 μM Calcein-AM and 8μM PI) was added into each well followed by fluorescence imaging.

QUANTIFICATION AND STATISTICAL ANALYSIS

GraphPad Prism 7.0 (GraphPad Software Inc., USA) was employed for statistical analyses and graphs collection. One-way ANOVA and Two-way ANOVA analysis of variance test was used, followed by Bonferroni multi-comparisons. A P value less than 0.05 was considered to be statistically significant. All Data were presented as means ± SD. All experiments were performed in triplicates and three replicates were conducted for each independent experiment. The statistical details of experiments can also be found in figure legends.